applied sciences

MDPI

Article

Sparsity-Based Nondestructive Evaluations of Downhole Casings Technique Using the Uniform Linear Array

Jingxin Dang [1], Ling Yang [2], Yan Zhou [3] and Bo Dang [2,*]

[1] School of Resources and Environment, University of Electronic Science and Technology of China, Chengdu 611731, China; 15029276190@163.com
[2] Shaanxi Key Laboratory of Measurement and Control Technology for Oil and Gas Wells, Xi'an Shiyou University, Xi'an 710065, China; lingyang2915@163.com
[3] School of Information Science and Technology, Northwest University, Xi'an 710127, China; yanzhou@nwu.edu.cn
* Correspondence: bodang521@126.com; Tel.: +86-029-8838-2648

Abstract: Borehole pulsed eddy-current (PEC) systems based on uniform linear multicoil arrays (ULMAs) perform efficient nondestructive evaluations (NDEs) of metal casings. However, the limited physical space of the borehole restricts the degrees of freedom (DoFs) of ULMAs to be less than the number of constraints, which leads to the difficulty of compensating for the differences in signals acquired by different receivers with different transmitting-to-receiving distances (TRDs), and thus limits the effectiveness of the ULMA system. To solve this problem, this paper proposes sparse linear constraint minimum variance (S-LCMV) for NDEs of downhole casings employing ULMAs. By transforming and characterizing the original PEC signal, it was observed that the signal power dramatically decreased with increasing Legendre polynomial stage, confirming that the signal was sparsely distributed over the Gauss–Legendre stages. Using this property, the S-LCMV cost function with reduced constraints was constructed to provide enough DoFs to accurately calculate the weight coefficients, thus improving the detection performance. The effectiveness of the proposed method was verified through field experiments on an 8-element ULMA installed in a borehole PEC system for NDEs of oil-well casings. The results demonstrate that the proposed method could improve the weighting effect by reducing the number of constraints by 70% while ensuring the approximation accuracy, which effectively improved the signal-to-noise ratio of the measured signals and reduced the computational cost by about 87.9%.

Keywords: borehole; pulsed eddy current techniques; nondestructive evaluation; uniform linear array

Citation: Dang, J.; Yang, L.; Zhou, Y.; Dang, B. Sparsity-Based Nondestructive Evaluations of Downhole Casings Technique Using the Uniform Linear Array. *Appl. Sci.* **2024**, *14*, 6588. https://doi.org/10.3390/app14156588

Academic Editor: Luis Javier Garcia Villalba

Received: 26 June 2024
Revised: 20 July 2024
Accepted: 27 July 2024
Published: 28 July 2024

1. Introduction

The eddy-current technique has been widely applied to resource exploration [1], environmental investigations [2], and stress measurements [3]. A variant of the eddy-current technique called the pulsed eddy-current (PEC) technique [4,5] has been widely adopted for the nondestructive evaluation (NDE) of wellbore casings because it accesses the target without making physical contact. Furthermore, it identifies cracks, pits, and corrosion in metallic infrastructures without requiring surface preparation [6–8]. Casing defects are evaluated from broad-frequency-range data considering the electrical and geometrical parameters of the individually estimated layer [9,10]. However, unlike surface measurements, NDEs of downhole casings are degraded by high temperatures and metal tool housings against high pressure, and the small operating space downhole can also limit the inspection results [11–13].

Considering the harsh environment of actual downhole detection, array-based PEC probes and corresponding novel signal processing methods have been proposed to improve the performance of the NDE of downhole casings. References [14–18] designed and controlled a transmitting array consisting of multiple transmitter coils to achieve magnetic

field focusing, thus enhancing the longitudinal resolution of the PEC inspection system. Similarly, the authors of [19,20] investigated the performance of downhole NDE using a receiving array consisting of multiple receiver coils with different transmitting-to-receiving distances (TRDs). The different TRDs resulted in "phase shifts" between the detection curves obtained from different receiving elements, which affected the accuracy of the NDE of downhole casings. To address this problem, the authors of [21] identified the correlations among the receiving elements and weighted the array output using the linear constrained minimum variance (LCMV)-based method, originally developed for radar and sonar detection. The LCMV-based method effectively eliminates the influence of the TRD on the array output. Reference [22] further applied the LCMV-based method to a downhole PEC detection system with a multiple-input-multiple-output (MIMO) structure by increasing the number of channels to reduce the system complexity while maintaining the performance. The above studies show that configuring the transmitting and receiving arrays as uniform linear multicoil arrays (ULMAs) and applying a corresponding signal-processing method can effectively improve the NDE performance and accuracy of downhole PEC systems.

Although ULMAs enable the NDE of downhole casings, their degrees of freedom (DoFs) are severely constrained within the limited physical space and borehole conditions in practical applications, thus introducing a pathological problem caused by the DoFs being much smaller than the number of constraints [23]. Using the standard LCMV method for array signal processing can make it difficult to obtain valid weight coefficients due to the irreversibility of the matrix. Diagonal loading (DL) [24–26] has been shown to help improve the computational accuracy of the weight coefficients, but it is an empirical value-based method with a computationally intensive process and is not practically usable. Recently, sparse optimization has been proven to be effective in reducing computational complexity and beneficial in solving underdetermined problems [27–29]. To prevent the DoFs falling below the number of constraints, we propose a sparsity-based method for the NDE of downhole casings using the ULMA. First, the ULMA-based borehole PEC signal model was constructed and the Gauss–Legendre quadrature representation of the PEC signal was obtained. Through the structural transformation of the PEC signal, it was observed that the signal power decreased significantly with the increase in the Legendre polynomial stage, and the sparsity of the PEC signal was then analyzed and proven. On this basis, the sparse linear constraint minimum variance (S-LCMV) method was proposed to provide sufficient DoFs to obtain the effective weight coefficients by reducing the number of constraints, thus avoiding the influence of the ill-posed problem on the calculation accuracy. The effectiveness of the proposed method was verified through field experiments on a ULMA in a borehole PEC system designed for the NDE of oil-well casings. The results show that the proposed method was able to eliminate the influence caused by the different TRDs on the inspection effect, and improved the accuracy of the NDE of the downhole casings. In addition, the proposed S-LCMV method had a higher signal-to-noise ratio (SNR) compared to the standard LCMV method and a lower computational cost compared to the DL method, providing practical usability.

The rest of this study is organized as follows. Section 2 presents the ULMA-based borehole PEC signal model and the Gauss–Legendre quadrature representation for borehole PEC signals. In Section 3, the sparsity of the PEC signal is analyzed and the cost function of the S-LCMV method is proposed. Simulation and experimental results are provided and analyzed in Section 4. Finally, we conclude the work in Section 5.

2. ULMA-Based Borehole PEC Signal Model

Consider a ULMA-based borehole PEC system equipped with a single transmitter and M receivers. The receivers, each composed of a coaxial coil wound around a soft magnetic core in a cylindrically layered medium, are separated by Δz. The electrical and geometrical parameters of each layer in the multilayered borehole PEC system are denoted as ε_j, μ_j, σ_j, and r_j ($j = 1, 2, \ldots J$) (see Figure 1). The magnetic core is considered as the innermost layer. The transmitter and M receivers, with N_T and N_R turns, respectively, are located in

the second layer. Note that all receivers have the same number of turns. When M is large, both N_R and N_T can be configured sufficiently small to diminish the TRD of each single receiver. The individual TRDs can then be ignored and approximated as a single value. Moreover, if the diameters of all coils are assumed sufficiently small, the source region can be considered as the second layer alone. The induced electromagnetic force (EMF) of the receiving coils is then related only to the vertical component of the magnetic field of the first layer (the magnetic core). The remaining layers (such as liquid mud, casing, and formation) are regarded as source-free regions.

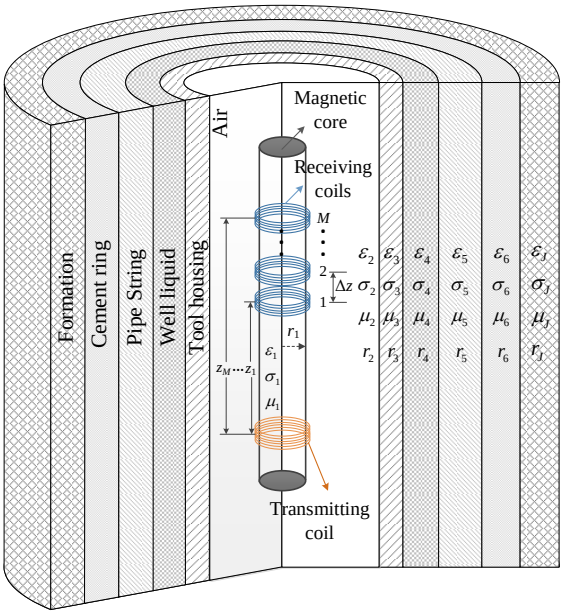

Figure 1. ULMA-based borehole PEC system.

When measuring the thickness of the metal pipes, we further assumed that the electrical parameters of all layers and the inner radius of the metal pipes were fixed. Considering one transmitter and M receivers with inter-element spacing Δz, the induced EMF in the m-th receiver can be calculated as [21]

$$U_m(t, z_m, d_m) = -\frac{\xi\chi}{t_{\text{of}}} \sum_{s=1}^{S} \sum_{q=1}^{Q} \sum_{p=1}^{P} g_{s,q,p}(t, d_m) v_p(z_m) \tag{1}$$

where $g_{s,\,q,\,p}(t, d_m) = D_s\{exp[(-\text{sln}2t_{of})/t]-1\}A_q(B_q+1)A_p x_1 C_1 I_0(x_1 r)/2s$, $v_p(z_m) = \cos[\lambda_0 z_m(B_p+1)/2]$, $\xi = \mu_1 N_R N_T I_T/\pi$, and $\chi = \pi {r_1}^2 \lambda_0/2$. In Equation (1), t and t_{of} denote the observation and turn-off times, respectively, z_m and d_m are the TRD and thickness of the metal casing with respect to the observation position of the m-th receiver, respectively, and S and D_s denote the stage and the integral coefficient of the Gaver–Stehfest inverse Laplace transform, respectively. P and Q represent the number of stages of the two Legendre polynomials with quadrature coefficient A and zero-point B. C_1 denotes the reflection coefficient in the innermost layer. x_j and λ are introduced variables satisfying ${x_j}^2 = \lambda^2 - {k_j}^2$. $I_0(\cdot)$ is a modified zero-order Bessel function of the first kind. Considering the monotonically decreasing characteristic of modified Bessel functions, we approximated the upper limit of integration of λ as λ_0. Note that $g_{s,q,p}(t, d_m)$ is related to s, q, and p whereas $v_p(z_m)$ is only related to p. Accordingly, Equation (1) can be concisely expressed as

$$U_m(t, z_m, d_m) = -\frac{\xi\chi}{t_{of}} \sum_{p=1}^{P} g_p(t, d_m) v_p(z_m) = -\frac{\xi\chi}{t_{of}} \mathbf{v}(z_m) \mathbf{g}^T(t, d_m) \tag{2}$$

where $\mathbf{g}(t, d_m) = [g_1(t, d_m), \ldots, g_p(t, d_m), \ldots, g_P(t, d_m)]$ with elements $g_p(t, d_m) = \sum_{s=1}^{S}\sum_{q=1}^{Q} g_{s,q,p}(t, d_m)$ and $\mathbf{v}(z_m) = [v_1(z_m), \ldots, v_p(z_m), \ldots, v_P(z_m)]$. As the receiver array is much shorter than the distance changes between two neighboring thicknesses, the thicknesses of the metal casing with respect to the observation position of each receiving coil are identical along the borehole axis, namely, $d_1 = d_2 = \ldots = d_M = d_0$. Considering the noise generated in each receiver, we stacked the EMFs induced in the M receivers into a vector as follows:

$$\mathbf{u}(t, d_0) = [U_1(t, z_1, d_0), \cdots, U_m(t, z_m, d_0), \cdots, U_M(t, z_M, d_0)]^T + \mathbf{n} = -\frac{\xi\chi}{t_{of}}\mathbf{V}\mathbf{g}^T(t, d_0) + \mathbf{n} \tag{3}$$

where $\mathbf{V} = [\mathbf{v}(z_1), \mathbf{v}(z_2), \ldots, \mathbf{v}(z_M)]^T$ and $\mathbf{n} = [n_1, n_2, \ldots, n_M]^T$ is a Gaussian white noise vector with a mean of 0 and a variance of σ^2. According to Equation (3), the phase varies with TRD, so the loss can be obtained by directly summing the EMFs [21]. To reduce the loss and ensure a satisfactory casing effect, the phase should be compensated and the noise should be suppressed. Therefore, the following LCMV cost function is established:

$$\begin{cases} \min \mathbf{w}^T\mathbf{R}_u\mathbf{w} \\ s.t.\ \mathbf{w}^T\mathbf{V} = \mathbf{f} \end{cases} \tag{4}$$

where $\mathbf{R}_u = E[\mathbf{u}\mathbf{u}^T]$ denotes the auto-correlation matrix of $\mathbf{u}$, and $\mathbf{f} = [1,1, \ldots, 1] \in \mathbb{Z}^{1\times P}$ is a row vector with all P elements equal to 1. The weight is optimized through the Lagrange multiplier methodology as

$$\mathbf{w} = \mathbf{R}_u^{-1}\mathbf{V}(\mathbf{V}^T\mathbf{R}_u^{-1}\mathbf{V})^{-1}\mathbf{f}^T \tag{5}$$

As shown in [21], Equation (5) can compensate for the phase shift at each receiver with a different TRD. The output SNR is then enhanced to improve the corresponding casing result. However, within the limited space of downhole casings, the number of receivers M is usually far smaller than P, so the number of constraints in Equation (4) is considerably larger than the dimension of $\mathbf{w}$, and the inverse of $\mathbf{V}^T{\mathbf{R}_u}^{-1}\mathbf{V}$ becomes ill-conditioned. Although the inverse of $\mathbf{V}^T{\mathbf{R}_u}^{-1}\mathbf{V}$ can be computed through the DL method, the selection of the DL factor is based on empirical values and the process entails a large number of calculations, making the method lack practical usability. To avoid the ill-conditioning of Equation (4) and improve the NDE effect, we established a sparsity-based cost function that reduced the number of constraints in Equation (4).

3. The Proposed S-LCMV Cost Function

This section analyzes the sparsity of $\mathbf{g}(t, d_m)$ in detail and reconstructs the corresponding cost function with a sparse $\mathbf{g}(t, d_m)$ to provide sufficient DoFs. Based on the aforementioned definition of the vector $\mathbf{g}(t, d_m)$, we fixed s and q in $g_{s,q,p}(t, d_m)$ to analyze the variation in the values of $g_{s,q,p}(t, d_m)$ with respect to the Legendre polynomial stage p. Referring to the expression of $g_{s,q,p}(t, d_m)$, we now examine the p-dependent variations of $A_p x_1 C_1 I_0(x_1 r)$. According to the boundary continuity condition, the important factor C_1 can be obtained as follows [30]:

$$C_1 = \mathbf{Y}_1(1,2) + \mathbf{Y}_2(1,1) + \mathbf{Y}_3(1,1) \tag{6}$$

$$\mathbf{Y}_1 = {\mathbf{A}_1}^{-1} \times \mathbf{B}_1 \times {\mathbf{A}_2}^{-1} \times \mathbf{B}_2 \times {\mathbf{A}_3}^{-1} \times \mathbf{B}_3 \times {\mathbf{A}_4}^{-1} \times \mathbf{B}_4 \times {\mathbf{A}_5}^{-1} \times \mathbf{B}_5 \times {\mathbf{A}_6}^{-1} \times \mathbf{B}_6 \tag{7}$$

$$\mathbf{Y}_2 = {\mathbf{A}_1}^{-1} \times \mathbf{B}_1 \times {\mathbf{A}_2}^{-1} \times \mathbf{O}_2 \tag{8}$$

$$\mathbf{Y}_3 = {\mathbf{A}_1}^{-1} \times \mathbf{O}_1 \tag{9}$$

where $\mathbf{Y}(i,j)$ denotes the element of matrix $\mathbf{Y}$ located in the i-th row and j-th column. The matrix ${\mathbf{A}_j}^{-1}$ represents the inverse of matrix $\mathbf{A}_j$ with

$$\mathbf{A}_j = \begin{bmatrix} \mu_j I_1(x_j r_j) & \mu_j K_1(x_j r_j) \\ x_j I_0(x_j r_j) & -x_j K_0(x_j r_j) \end{bmatrix} \tag{10}$$

$$\mathbf{B}_j = \begin{bmatrix} \mu_{j+1} I_1(x_{j+1} r_j) & \mu_{j+1} K_1(x_{j+1} r_j) \\ x_{j+1} I_0(x_{j+1} r_j) & -x_{j+1} K_0(x_{j+1} r_j) \end{bmatrix} \tag{11}$$

$$\mathbf{O}_1 = \begin{bmatrix} \mu_2 K_1(x_2 r_0) I_1(x_2 r_0) \\ x_2 K_1(x_2 r_0) I_0(x_2 r_0) \end{bmatrix} \tag{12}$$

$$\mathbf{O}_2 = \begin{bmatrix} -\mu_2 K_1(x_2 r_0) I_1(x_2 r_0) \\ x_2 K_0(x_2 r_0) I_1(x_2 r_0) \end{bmatrix} \tag{13}$$

In the above equations, $I_0(xr)$ = *besseli*(0, xr) and $I_1(xr)$ = *besseli*(1, xr) are modified Bessel functions of the first kind with order 0 and order1, respectively. $K_0(xr)$ = *besselk*(0, xr) and $K_1(xr)$ = *besselk*(1, xr) are modified Bessel functions of the second kind with order 0 and order1, respectively. When p becomes sufficiently large, $\lambda >> k_j$, then we have $x_j = (\lambda^2 - k_j^2)^{1/2} \approx \lambda$, $I_1(x_j r_j) \approx I_1(x_{j+1} r_j)$, $K_1(x_j r_j) \approx K_0(x_j r_j)$, $I_0(x_j r_j) \approx I_0(x_{j+1} r_j)$, and $K_0(x_j r_j) \approx K_0(x_{j+1} r_j)$. For further analysis, we show the distributions of the Bessel functions in Figure 2. The Bessel functions of the first and second kinds exponentially grow and decay, respectively, with increasing parameter xr. Therefore, when λ is large (i.e., the stage of the Gauss–Legendre integral is high or p is large), the elements in the second row of $\mathbf{A}_j^{-1}$ and the elements in the first column of $\mathbf{B}_j$ are dominant, while the other elements are negligibly small (approximately zero).

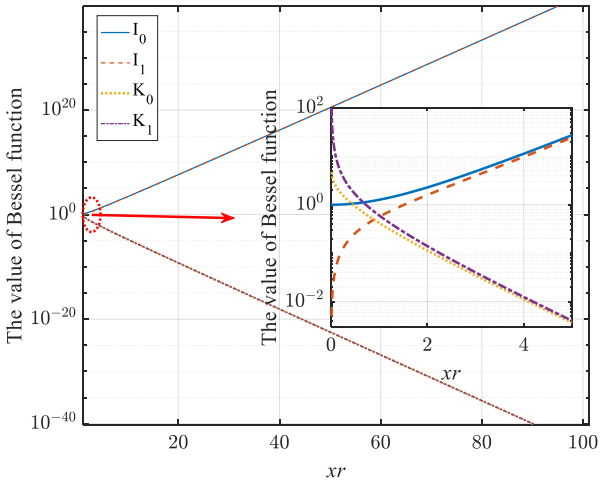

Figure 2. Distribution of Bessel functions.

To facilitate the analysis, the variables α, β, a, and b are introduced to further simplify the expression. Assuming that α and β are infinitesimally small (approaching zero) and much smaller than a and b, the elements in $\mathbf{A}_j^{-1}$ and $\mathbf{B}_j$ can be expressed as

$$\mathbf{A}_j^{-1} = \begin{bmatrix} \alpha_j' & \alpha_j'' \\ a_j' & a_j'' \end{bmatrix} \tag{14}$$

$$\mathbf{B}_j = \begin{bmatrix} b_j' & \beta_j' \\ b_j'' & \beta_j'' \end{bmatrix} \tag{15}$$

which multiply to give

$$\mathbf{AB}_j = \mathbf{A}_j^{-1} \times \mathbf{B}_j = \begin{bmatrix} \alpha_j' & \alpha_j'' \\ a_j' & a_j'' \end{bmatrix} \begin{bmatrix} b_j' & \beta_j' \\ b_j'' & \beta_j'' \end{bmatrix} = \begin{bmatrix} \alpha_j' b_j' + \alpha_j'' b_j'' & \alpha_j' \beta_j' + \alpha_j'' \beta_j'' \\ a_j' b_j' + a_j'' b_j'' & a_j' \beta_j' + a_j'' \beta_j'' \end{bmatrix} \tag{16}$$

Accordingly, we have $\mathbf{Y}_1 = \mathbf{AB}_1 \times \mathbf{AB}_2 \times \mathbf{AB}_3 \times \mathbf{AB}_4 \times \mathbf{AB}_5 \times \mathbf{AB}_6$. Since α_j', α_j'', β_j', and β_j'' are all infinitesimals, their products are also infinitesimals. To simplify the subsequent expres-

sions, let γ_j', γ_j'', and γ_j''' denote the three infinitesimals in $\mathbf{AB}_j$, and let c_j denote the constant term in $\mathbf{AB}_j$, then we have

$$\mathbf{AB}_1 \times \mathbf{AB}_2 = \begin{bmatrix} \gamma_1' & \gamma_1'' \\ c_1 & \gamma_1''' \end{bmatrix} \begin{bmatrix} \gamma_2' & \gamma_2'' \\ c_2 & \gamma_2''' \end{bmatrix} = \begin{bmatrix} \gamma_1'\gamma_2' + \gamma_1''c_2 & \gamma_1'\gamma_2'' + \gamma_1''\gamma_2''' \\ c_1\gamma_2' + \gamma_1'''c_2 & c_1\gamma_2'' + \gamma_1'''\gamma_2''' \end{bmatrix} \tag{17}$$

$$\mathbf{AB}_3 \times \mathbf{AB}_4 = \begin{bmatrix} \gamma_3'\gamma_4' + \gamma_3''c_4 & \gamma_3'\gamma_4'' + \gamma_3''\gamma_4''' \\ c_3\gamma_4' + \gamma_3'''c_4 & c_3\gamma_4'' + \gamma_3'''\gamma_4''' \end{bmatrix} \tag{18}$$

$$\mathbf{AB}_5 \times \mathbf{AB}_6 = \begin{bmatrix} \gamma_5'\gamma_6' + \gamma_5''c_6 & \gamma_5'\gamma_6'' + \gamma_5''\gamma_6''' \\ c_5\gamma_6' + \gamma_5'''c_6 & c_5\gamma_6'' + \gamma_5'''\gamma_6''' \end{bmatrix} \tag{19}$$

Furthermore, we can obtain

$$\begin{aligned} \mathbf{Y}_1(1,2) \quad &= \left[(\gamma_1'\gamma_2' + \gamma_1''c_2)(\gamma_3'\gamma_4' + \gamma_3''c_4) + (\gamma_1'\gamma_2'' + \gamma_1''\gamma_2''')(c_3\gamma_4' + \gamma_3'''c_4)\right](\gamma_5'\gamma_6'' + \gamma_5''\gamma_6''') \\ &+ \left[(c_1\gamma_2' + \gamma_1'''c_2)(\gamma_3'\gamma_4'' + \gamma_3''\gamma_4''') + (c_1\gamma_2'' + \gamma_1'''\gamma_2''')(c_3\gamma_4'' + \gamma_3'''\gamma_4''')\right](c_5\gamma_6'' + \gamma_5'''\gamma_6''') \end{aligned} \tag{20}$$

According to Equation (20), it can be seen that $\mathbf{Y}_1(1, 2)$ is an infinitesimal quantity. Similarly, as the multiplication product of the modified Bessel functions of the first and second kinds approaches zero when λ is large, the elements in $\mathbf{Y}_2(1, 1)$ and $\mathbf{Y}_3(1, 1)$ are also infinitesimal. Meanwhile, as A_p, D_s, and B_q, are all normal constants in $g_{s,q,p}(t, d_m)$, $g_{s,q,p}(t, d_m)$ will follow C_1 to become infinitesimally small when p becomes large. Then, the sum of a finite number of infinitesimal quantities, namely, $g_p(t, d_m) = \sum_{s=1}^{S}\sum_{q=1}^{Q} g_{s,q,p}(t, d_m)$, also becomes an infinitesimal quantity. The above analysis shows that the value of $g_{s,q,p}(t, d_m)$ is dominated by only a small subset of $g_{s,q,p}(t, d_m)$, and the term $\mathbf{g}(t, d_m)$, containing the wall thickness information, possesses an obvious sparse property. The sparse structure of $\mathbf{g}(t, d_m)$ is presented in the experimental section for ease of understanding

Based on the above discussion, it can be concluded that for large p, $g_p(t, d_m)$ is an infinitesimal quantity that minimally contributes to the received signal $U_m(t, z_m, d_m)$. Consequently, sparse constraints corresponding to the dominant $g_p(t, d_m)$ are imposed and the S-LCMV cost function is formulated as

$$\begin{cases} \min \mathbf{w}_s^T \mathbf{R}_{u_s} \mathbf{w}_s \\ s.t.\ \mathbf{w}_s^T \mathbf{V}_K = \mathbf{f}_K \end{cases} \tag{21}$$

where $\mathbf{V}_K = [\mathbf{v}'(z_1), \mathbf{v}'(z_2), \ldots, \mathbf{v}'(z_M)]^T$, $\mathbf{v}'(z_m) = [v_1(z_m), \ldots, v_k(z_m), \ldots, v_K(z_m)]$, $\mathbf{f}_K = [1,1, \ldots, 1] \in \mathbb{Z}^{1\times K}$ with $K < P$, and $\mathbf{R}_{us} = E[\widetilde{\mathbf{u}}\widetilde{\mathbf{u}}^T]$ denotes the auto-correlation matrix of $\widetilde{\mathbf{u}}$. Each element in $\widetilde{\mathbf{u}}$ is expressed as

$$\widetilde{U}_m(t, z_m, d_0) = -\frac{\xi\chi}{t_{\text{of}}} \sum_{k=1}^{K} g_k(t, d_m) v_k(z_m) \tag{22}$$

Equation (21) is then solved as

$$\mathbf{w}_s = \mathbf{R}_{u_s}^{-1}\mathbf{V}_K(\mathbf{V}_K^T\mathbf{R}_{u_s}^{-1}\mathbf{V}_K)^{-1}\mathbf{f}_K{}^T \tag{23}$$

Due to the sparsity of $\mathbf{g}(t, d_m)$, K is much smaller than P. In particular, numerical simulations confirmed that $K < M < P$, meaning that the number of constraints was fewer than the DoFs in the adaptive weight function. In this case, $\mathbf{V}_K{}^T\mathbf{R}_{us}{}^{-1}\mathbf{V}_K$ will become well-conditioned and invertible. Accordingly, accurate weight coefficients can be calculated and the inspection effect can be improved effectively.

In addition, solving Equation (23) incurs a much lower computational cost than solving Equation (5) because it involves a small-scale matrix multiplication. To evaluate the computational cost in quantity, we adopted the multiplication and division number

(MDN) [31]. Note that the MDN of an $M \times M$ matrix inverse is approximately $2M^3/3$, and that of multiplying an $M \times N$ matrix by an $N \times H$ matrix is MNH. Therefore, we have

$$MDN_{S-LCMV} = \frac{2}{3}(M^3 + K^3) + KM(K + M) + K^2 + MK + M^2 \quad (24)$$

$$MDN_{LCMV} = \frac{2}{3}(M^3 + P^3) + PM(P + M) + P^2 + MP + M^2 \quad (25)$$

where $MDN_{S\text{-}LCMV}$ and MDN_{LCMV} represent the MDNs of solving Equations (23) and (5), respectively. Evidently, $MDN_{S\text{-}LCMV}$ is considerably smaller than MDN_{LCMV} when $K << P$. The above study shows that the PEC signal exhibits sparsity depending on the Gauss–Legendre stage p, which is employed to construct an S-LCMV method that can accurately calculate the weighting coefficients and thus effectively eliminate the interference of the different TRDs on the detection effect. Moreover, the proposed method can also greatly reduce the computational cost. The practical effectiveness of the proposed approach will be verified by simulation experiments in the next section.

4. Simulation Experiments

The ULMA-based borehole PEC system for downhole casing inspections was validated through field experiments conducted in standardized $5^{1/2}$-inch metal casings (thickness 7.72 mm; outer diameter 139.7 mm). To illustrate the effectiveness of the proposed method, the thickness of the metal casing was changed to varying degrees from the nominal thickness, with wall thickness variations from top to bottom of 3 mm, 1 mm, 2 mm, and 4 mm, corresponding to the lengths of the varied segments of 15 cm, 10 cm, 10 cm, and 15 cm, respectively (as shown in Figure 3). Standard PEC measurements of the above metal casing were performed using an 8-element linear multicoil array in accordance with the standardized experimental procedure. The relevant models and experimental results were processed using the MATLAB platform on a system using a 16-core processor with 32 GB of RAM and a 1 TB hard disk. The parameters of the experiment and the multicoil array sensor are listed in Table 1.

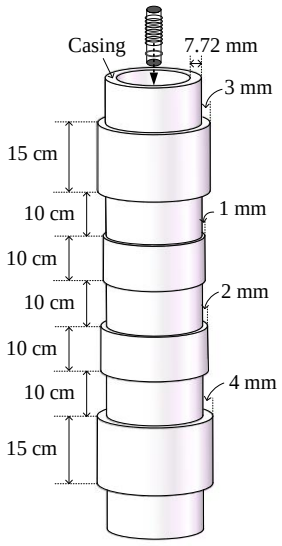

Figure 3. Configuration of the experimental metal casing.

Table 1. Parameters of the simulation experiment.

Parameters	Symbol	Value
Number of receiving coils	M	8
Inter-element spacing	Δz	20 mm
Transmitting–receiving distances	$z_1 - z_M$	20–160 mm

Table 1. *Cont.*

Parameters	Symbol	Value
Number of transmitting coil turns	N_T	19
Number of receiving coil turns	N_R	62
Radius of the multicoil array sensor	r_1	12 mm
Tool housing inner radius	r_2	18.5 mm
Tool housing outer radius	r_3	21.5 mm
Standardized casing inner radius	r_4	62.13 mm
Standardized casing outer radius	r_5	69.85 mm
Cement ring outer radius	r_6	88.9 mm
Excitation current	I_T	0.3 A
Observation time interval	t	0–50 ms
Step size	Δt	1 ms

By analyzing the PEC signals in this experiment, the distribution of each element in $\mathbf{g}(t, d_m)$ (normalized by the maximum value) as a function of p is obtained, as shown in Figure 4a. It can be seen that the term $\mathbf{g}(t, d_m)$ decays in an exponential-like manner as the stage p increases (i.e., the signal characteristics are dominated by the first several elements), verifying that $\mathbf{g}(t, d_m)$ is sparse. To make it easier to understand, we provide the percentage contribution of each element with different p-values to the overall signal power (as shown in Figure 4(b)). Obviously, for the vector $\mathbf{g}(t, d_m)$, the contribution of the first eight elements could account for more than 90%, while the contribution of the other elements was basically negligible. Therefore, by exploiting this property, it is possible to reduce the number of constraints from P to K, thus providing enough DoFs to obtain accurate weight coefficients. Initially, we determined $K < 8$ to avoid the pathological problems that would lead to the failure of the weight coefficients. Combining the balanced relationship between model approximation accuracy and computational cost, the original full-dimensional LCMV with $P = 20$ could be reduced to an S-LCMV with $K = 6$ in this experiment. In other words, the number of constraints was reduced by 70% from P for LCMV to K for S-LCMV. In addition, according to the relevant definitions in Equations (24) and (25) in Section 3, the proposed method was capable of reducing the computational cost by about 87% from the original. It should be noted that the selection of the value of K is mainly related to the calculation accuracy of the weight coefficients and the model approximation accuracy. Specifically, the larger the value of K, the more the signal model approximates the actual situation, but it introduces a larger amount of computation, and even when $K > M$, it is difficult to obtain effective weight coefficients. Conversely, the smaller the value of K, the amount of computation is greatly reduced, which is conducive to the accurate calculation of the weight coefficients, however, an excessively small K leads to a large deviation between the signal model and the actual signal, thus creating a large inspection error. Therefore, the selection of K is the process of realizing the balance between the calculation accuracy of the weight coefficients, the calculation speed, and the model approximation accuracy.

To analyze the performance of the proposed method, we processed the measured data using the standard LCMV algorithm, the DL-based method, the MIMO-based method, and the proposed S-LCMV algorithm. Figures 5 and 6 show the weighted-sum results of the 8-element ULMA at late and early times, respectively. As can be seen from Figures 5a and 6a, due to the sufficient DoFs for controlling the constraints in S-LCMV, it was possible to obtain an accurate and effective weighting coefficient $\mathbf{w}_s$, which could well compensate for the phase differences between the receivers and formed a smooth EMF curve for detection. Note that the amplitude of the weighted induced EMFs monotonically increased with the thickness of the metal pipe, revealing a relationship between the induced EMFs and pipe thickness. In contrast, for the standard LCMV algorithm (shown in Figures 5b and 6b), it was difficult to obtain the accurate weighting coefficient $\mathbf{w}$ because Equation (5) included an excessive number of constraints, resulting in poor compensation of the phase difference between the receivers. Figures 5c and 6c demonstrate the processing results of the MIMO-based method. It can be seen that the method improved the weighted-sum effect

compared to the standard LCMV, but its consistency with the actual casing variation was not high enough. In addition, due to the structure of the probe with multiple transmitters and multiple receivers, the large TRD made the SNR of the signal poor, and the EMF curve was not smooth enough. Moreover, Figures 5d and 6d demonstrate the experimental results of the DL-based method. It can be seen that the DL-based method could improve the detection effect and obtained a similar performance as the S-LCMV algorithm. However, DL is an empirical-value-based method with a complicated process and tends to result in a huge computational volume, making it not practically usable. In comparison, the S-LCMV algorithm is not only able to avoid the pathological problem by exploiting the sparsity characteristics of the signals, but also possesses strong practical usability, which effectively achieves a good application of array weighting in downhole signal models.

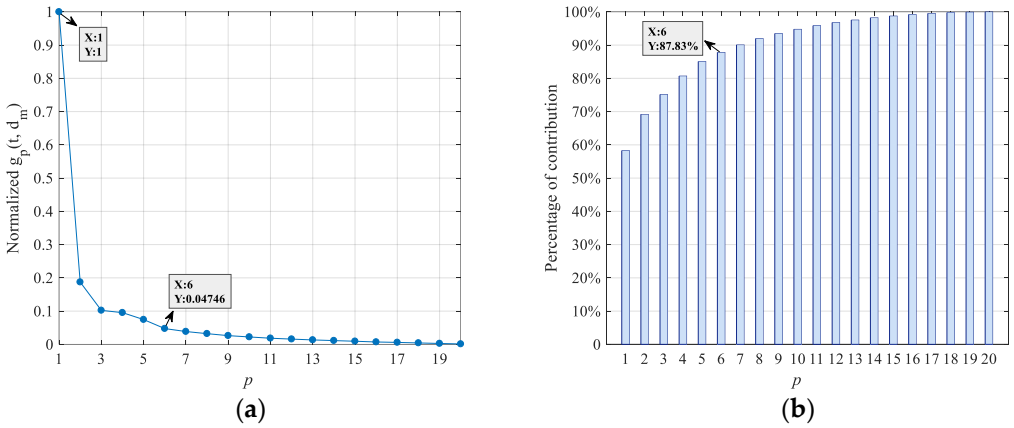

Figure 4. The sparsity of $\mathbf{g}(t, d_m)$. (**a**) Normalized $\mathbf{g}(t, d_m)$; (**b**) percentage contribution of each element.

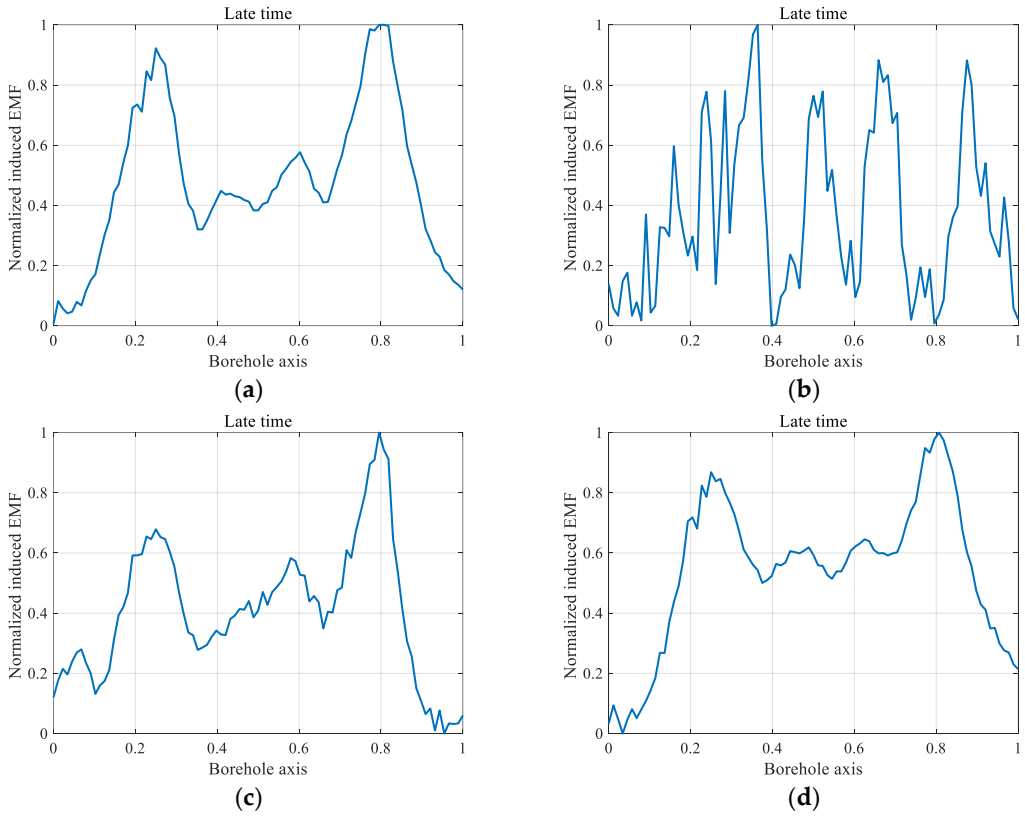

Figure 5. Weighted induced EMFs of an 8-receiver linear multicoil array at a late time. (**a**) S-LCMV; (**b**) LCMV; (**c**) MIMO; (**d**) DL.

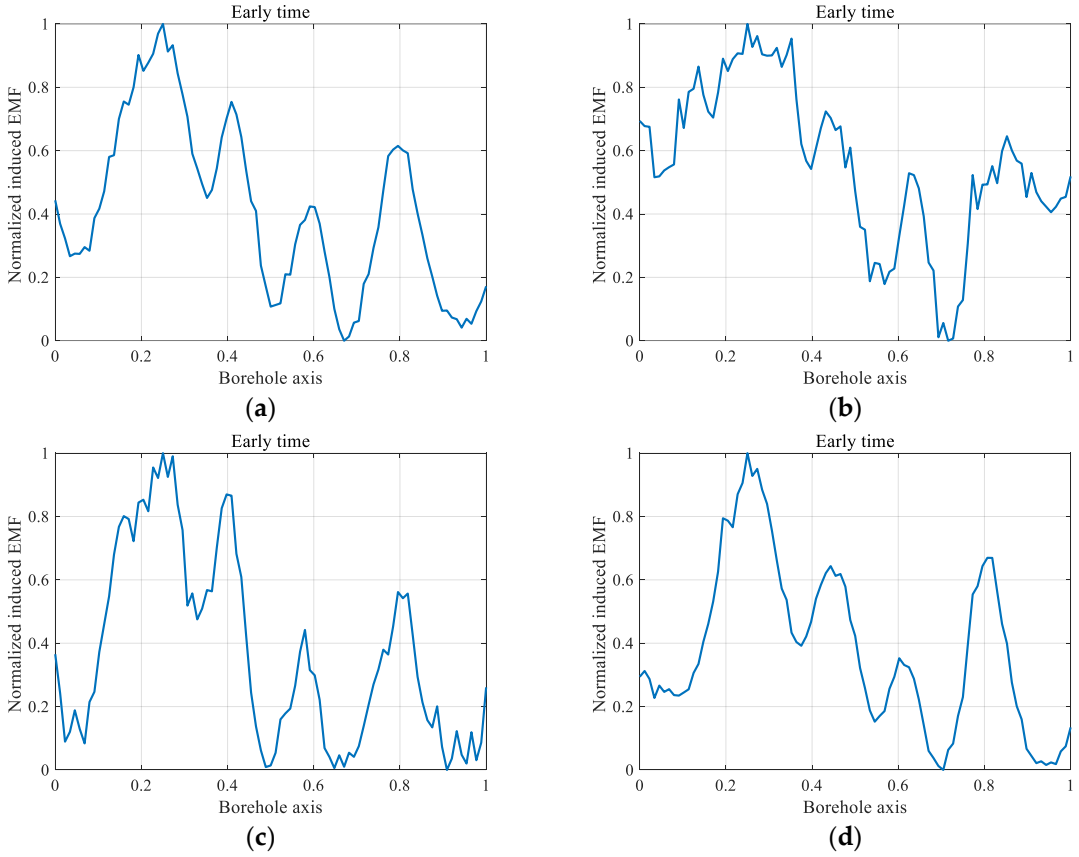

Figure 6. Weighted induced EMFs of an 8-receiver linear multicoil array at an early time. (**a**) S-LCMV; (**b**) LCMV; (**c**) MIMO; (**d**) DL.

After obtaining the weighted sum of the induced EMFs, the detection curves needed to be further interpreted to obtain the number and location(s) of the casing changes. For the data processed by the three different methods above-mentioned, the constant false alarm rate (CFAR) [32,33] detector, which is frequently used for target detection, was employed, and the detection results are demonstrated in Figures 7 and 8. Figures 7a and 8a demonstrate the CFAR detection results based on the proposed S-LCMV method with $\mathbf{w}_S$, where four target regions (in which the pipe was thicker than the nominal pipe) were clearly detected and their corresponding positions and sizes were highly consistent with the actual situation. When CFAR detection was performed using data processed by standard LCMV with $\mathbf{w}$, it was found that the number and location of targets could not be accurately obtained and the detection was ineffective (as shown in Figures 7b and 8b). In addition, the CFAR detection results of the data processed by the MIMO-based method are shown in Figures 7c and 8c. Although the corresponding detection results improved compared with the LCMV, the detection performance was still worse than the S-LCMV and it was difficult to accurately reflect the real situation of the casing changes. It should be noted that the detection results of CFAR based on S-LCMV were highly consistent with the actual pipeline damage locations, but there was still a certain degree of deviation from the actual because a known statistical distribution of noise is required to be assumed in typical radar systems, which may not be applicable to borehole casing. The above results validate that the CFAR is suitable for pipeline damage location detection, and the design of an improved CFAR detector to accurately detect both the number and location of targets in borehole application will be the focus of our future work.

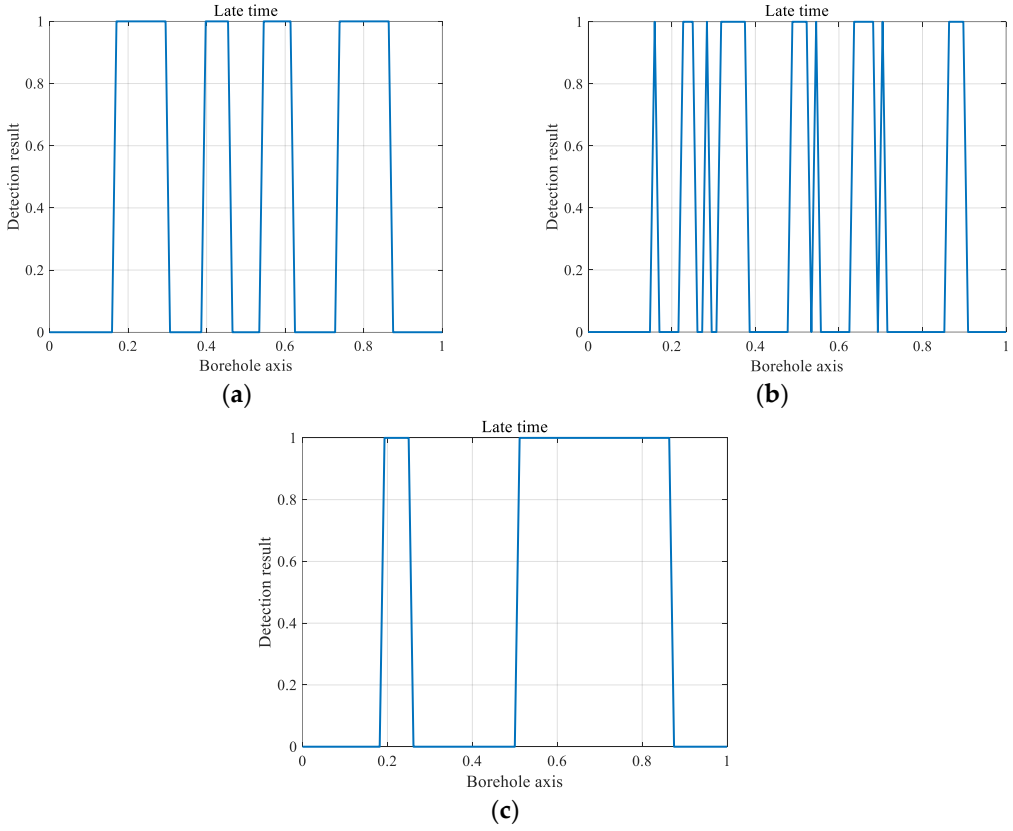

Figure 7. CFAR results of target detection at the late time. (**a**) S-LCMV; (**b**) LCMV; (**c**) MIMO.

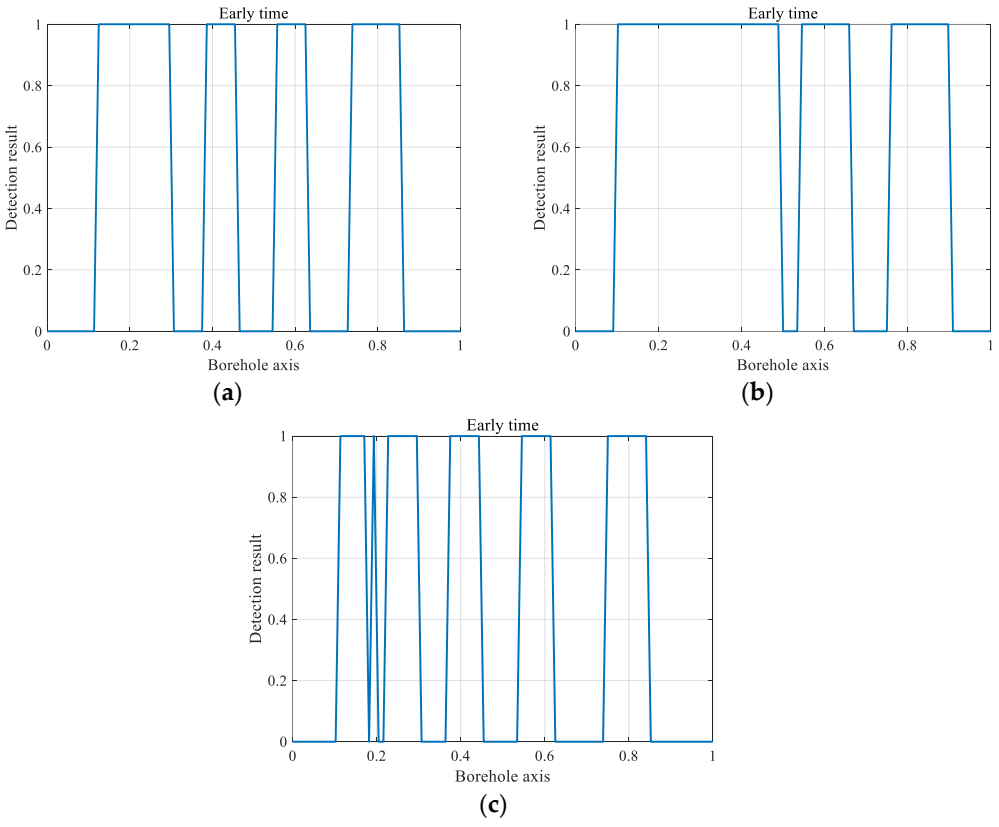

Figure 8. CFAR results of target detection at an early time. (**a**) S-LCMV; (**b**) LCMV; (**c**) MIMO.

As a result of the above analyses, the S-LCMV algorithm is conducive to obtaining accurate detection results in practical applications, which can reduce the calculation cost in the signal processing process and effectively improve the inspection efficiency and accuracy. In practical applications, the proposed method may face some challenges due to the complexity and uncertainty of the downhole environment. On the one hand, when the downhole physical space is very limited and the number of array elements is required to be further reduced, the corresponding reduction in the value of K may make the model approximation error too large due to the small stage of the Legendre polynomials, resulting in unreliable detection results. In this case, further exploitation of the sparsity of PEC signals can be considered to introduce emerging signal processing techniques such as a compressive sensing method with dimensionality reduction properties to ensure detection performance, which will be thoroughly investigated as a new research direction in future work. On the other hand, the multi-layer cylindrical structure involves numerous structural and electromagnetic parameters, while the uncertainties in the downhole environment make it difficult to ensure the accuracy of these parameters, which in turn affects the effectiveness of the proposed method. To decrease the sensitivity of the proposed method to the errors of the background medium parameters, in future research, we will consider integrating some cumulant algorithms to achieve adaptive weighting, thus further improving the robustness of the method.

5. Conclusions

This study established an S-LCMV method that reduces the number of constraints to below the DoFs in a ULMA system. The correlation between the PEC signal power and Legendre polynomial stages revealed sparsity of the signal with respect to the Gauss–Legendre stage. The S-LCMV provides an adequate number of DoFs under the imposed constraints, making it possible to accurately obtain valid weights, thus mitigating the influence of TRDs at different array elements. In addition, the number and locations of the casing-thickness changes were evaluated using the CFAR indicator, enabling rapid and intuitive nondestructive evaluations for downhole casings. Simulation and field experiments confirmed the superiority of S-LCMV over LCMV, which not only reduced the computational cost of the weights, but also improved the computational speed and accuracy in spite of the deviation of the borehole axis from the true axis. In future work, we will design an improved CFAR detector that accurately detects both the number and location of targets in borehole applications.

Author Contributions: Conceptualization, L.Y.; Methodology, B.D.; Software, L.Y.; Validation, J.D.; Formal analysis, Y.Z.; Investigation, J.D.; Resources, B.D.; Data curation, Y.Z.; Writing—original draft preparation, J.D.; Writing—review and editing, J.D.; Visualization, L.Y.; Supervision, Y.Z.; Project administration, B.D.; Funding acquisition, B.D. All authors have read and agreed to the published version of the manuscript.

Funding: This work was sponsored by the National Natural Science Foundation of China [grant numbers 51974250, 61901371]; the Youth Science and Technology Nova Project in Shaanxi Province, China [grant number 2020KJXX-018]; the Natural Science Basic Research Program of Shaanxi [grant number 2024JC-YBMS-522]; the Youth Scientific Research and Innovation Team Construction Plan Project of Xi'an Shiyou University [grant number 2022QNKYCXTD02]; and China Postdoctoral Science Foundation [grant number 2020M683541].

Institutional Review Board Statement: Not applicable.

Informed Consent Statement: Not applicable.

Data Availability Statement: All the details of this work including the data and algorithm codes are available by contacting the corresponding author: bodang521@126.com.

Acknowledgments: The authors would like to thank the reviewers for their helpful suggestions, which have considerably improved the quality of the manuscript.

Conflicts of Interest: The authors declare no conflicts of interest.

Notation List

$\mathbf{a}$	The vector $\mathbf{a}$
$\mathbf{A}$	The matrix $\mathbf{A}$
a_n	The n-th entry of a
$\mathbf{A}(m, n)$	The element of matrix $\mathbf{A}$ located in the m-th row and n-th column
$(\cdot)^T$	The transpose operator
$(\cdot)^{-1}$	The inverse operator
$\mathbb{Z}^{M\times N}$	The $M \times N$ integer-valued matrix
$E[\cdot]$	The statistical expectation
$\sum_{n=1}^{N}$	$a_1 + a_2 + \ldots + a_N$
$\exp(x)$	Exponential function of x
$\ln x$	Natural logarithm of x
$\mathbf{A} \times \mathbf{B}$	Matmul product of $\mathbf{A}$ and $\mathbf{B}$
besseli $(\cdot)$	The modified Bessel function operator of the first type
besselk $(\cdot)$	The modified Bessel function operator of the second type

References

1. Wang, S.; Guo, Y.; Li, D. Characteristics of new permanent magnetic eddy current drive system of the scraper conveyor. *J. Eng.* **2021**, *10*, 552–558. [CrossRef]
2. Wang, W.; Dalton, D.; Hua, X.; Wang, X.; Chen, Z.; Song, G. Experimental Study on Vibration Control of a Submerged Pipeline Model by Eddy Current Tuned Mass Damper. *Appl. Sci.* **2017**, *7*, 987. [CrossRef]
3. Habibalahi, A.; Moghari, M.; Samadian, K.; Mousavi, S.; Safizadeh, M. Improving pulse eddy current and ultrasonic testing stress measurement accuracy using neural network data fusion. *IET Sci. Meas. Technol.* **2015**, *9*, 514–521. [CrossRef]
4. Xiong, J.; Liang, W.; Ding, Y.; Yao, J. Quantitative analysis of wall thinning of bimetallic clad steel tube based on pulsed eddy current. *Process Saf. Prog.* **2022**, *41*, S118–S128. [CrossRef]
5. Sun, H.; Shi, Y.; Zhang, W.; Li, Y. Transient eddy current response to pulsed eddy current testing inside a ferromagnetic casing. *NDT E Int.* **2022**, *126*, 102587. [CrossRef]
6. Ona, D.I.; Tian, G.Y.; Sutthaweekul, R.; Naqvi, S.M. Design and optimisation of mutual inductance based pulsed eddy current probe. *Measurement* **2019**, *144*, 402–409. [CrossRef]
7. Wang, Y.; Nie, Y.; Qi, P.; Zhang, N.; Ye, C. Inspection of Defect Under Thick Insulation Based on Magnetic Imaging with TMR Array Sensors. *IEEE Trans. Magn.* **2021**, *58*, 1–10. [CrossRef]
8. Rifai, D.; Abdalla, A.; Razali, R.; Ali, K.; Faraj, M. An Eddy Current Testing Platform System for Pipe Defect Inspection Based on an Optimized Eddy Current Technique Probe Design. *Sensors* **2017**, *17*, 579. [CrossRef]
9. Ding, S.; Tian, G.; Zhu, J.; Chen, X.; Wang, Y.; Chen, Y. Characterisation and evaluation of paint-coated marine corrosion in carbon steel using eddy current pulsed thermography. *NDT E Int.* **2022**, *130*, 102678. [CrossRef]
10. Yu, X.; Zhu, Y.; Cao, Y.; Xiong, J. Time-Domain Numerical Simulation and Experimental Study on Pulsed Eddy Current Inspection of Tubing and Casing. *Sensors* **2023**, *23*, 1135. [CrossRef]
11. Abubakirov, R.; Yang, M.; Khakzad, N. A risk-based approach to determination of optimal inspection intervals for buried oil pipelines. *Process Saf. Environ.* **2020**, *134*, 95–107. [CrossRef]
12. Zhou, D.; Wang, J.; He, Y.; Chen, D.; Li, K. Influence of metallic shields on pulsed eddy current sensor for ferromagnetic materials defect detection. *Sens. Actuator A Phys.* **2016**, *248*, 162–172. [CrossRef]
13. Chen, X.; Niu, H. Pulsed eddy current testing for gap measurement of metal casing. *Meas. Sci. Technol.* **2022**, *7*, 33. [CrossRef]
14. Liu, C.; Dang, B.; Wang, H.; Shen, X.; Yang, L.; Ren, Z.; Dang, R.; Kang, Y.; Sun, B. Multiple-Transmit Focusing for the Nondestructive Testing of Downhole Casings Based on Borehole Transient Electromagnetic Systems. *IEEE Access* **2020**, *8*, 210978–210987. [CrossRef]
15. Choi, B.; Kim, J.; Cheon, J.; Rim, C. Synthesized magnetic field focusing using a current-controlled coil array. *IEEE Magn. Lett.* **2016**, *7*, 1–4. [CrossRef]
16. Liu, C.; Dang, B.; Wang, H.; Yang, L.; Dang, J.; Shen, X.; Dang, R. Synthesized Magnetic Field Focusing for the Non-Destructive Testing of Oil and Gas Well Casing Pipes Using Pulsed Eddy-Current Array. *IEEE Trans. Magn.* **2022**, *58*, 6201710. [CrossRef]
17. Kim, J.; Choi, B.; Kim, H.; Rim, C.; Kim, Y. Single-variable-input active sidelobe suppression method for synthesized magnetic field focusing technology and its optimization. *IEEE Trans. Ind. Electron.* **2020**, *67*, 9813–9823. [CrossRef]
18. Yang, L.; Liu, C.; Dang, J.; Zhao, Y.; Dang, B.; Dang, R. Synthesized Transmitting Coil for Magnetic Focusing of Pulsed Eddy Current for Downhole Casing Inspection. *Appl. Sci.* **2022**, *12*, 7695. [CrossRef]
19. Lahrech, A.; Naidjate, M.; Helifa, B.; Zaoui, A.; Abdelhadi, B.; Lefkaier, I.; Feliachi, M. Development of an axial rotating magnetic field multi-coil eddy current sensor for electromagnetic characterization of stratified CFRP materials. *NDT E Int.* **2022**, *126*, 102589. [CrossRef]
20. Song, Y.; Wu, X. An analytical solution for vertical coils near a multi-layered metallic pipe in Pulsed Eddy Current Testing. *NDT E Int.* **2022**, *125*, 102570. [CrossRef]

21. Dang, B.; Yang, L.; Liu, C.; Zhen, Y.; Li, H.; Dang, R.; Sun, B. A Uniform Linear Multi-Coil Array-Based Borehole Transient Electromagnetic System for Non-Destructive Evaluations of Downhole Casings. *Sensors* **2018**, *18*, 2707. [CrossRef] [PubMed]
22. Liu, C.; Dang, J.; Yang, L.; Zhou, Y.; Luo, X.; Dang, B. Space–Time Pulsed Eddy Current Array for NDT of Wellbore Casings Based on MIMO Technique. *IEEE Trans. Instrum. Meas.* **2024**, *73*, 1–12. [CrossRef]
23. Dang, J.; Yang, L.; Qin, C.; Zhao, Q.; Ji, X.; Guo, C.; Dang, B. Accurate ranging of adjacent well using compressive sensing-based current injection with a uniform sensor array. *Geoenergy Sci. Eng.* **2024**, *233*, 212468. [CrossRef]
24. Mestre, X.; Lagunas, M.A. Finite sample size effect on minimum variance beamformers: Optimum diagonal loading factor for large arrays. *IEEE Trans. Signal. Proces.* **2006**, *54*, 69–82. [CrossRef]
25. Muhammad, M.; Li, M.; Abbasi, Q.H.; Goh, C.; Imran, M.A. Adaptive Diagonal Loading Technique to Improve Direction of Arrival Estimation Accuracy for Linear Antenna Array Sensors. *IEEE Sens. J.* **2022**, *22*, 10986–10994. [CrossRef]
26. Elnashar, A.; Elnoubi, S.M.; El-Mikati, H.A. Further Study on Robust Adaptive Beamforming with Optimum Diagonal Loading. *IEEE Trans. Antenn. Propag.* **2006**, *54*, 3647–3658. [CrossRef]
27. Wang, P.; Venkataramanan, L.; Jain, V. Sparse Clustered Bayesian-Inspired T-T Inversion from Borehole NMR Measurements. *IEEE Trans. Comput.* **2017**, *3*, 355–368. [CrossRef]
28. Gholami, A.; Siahkoohi, H.R. Regularization of linear and non-linear geophysical ill-posed problems with joint sparsity constraints. *Geophys. J. Int.* **2010**, *180*, 871–882. [CrossRef]
29. Zhang, Y.; Zhang, G.; Kong, Y.; Wen, F. Gridless sparsity-based DOA estimation for sparse linear array. *J. Eng.* **2019**, *2019*, 6629–6632. [CrossRef]
30. Xu, J. *Electromagnetic Field and Electromagnetic Wave in Layered Media*; Petroleum Industry: Beijing, China, 1997; pp. 1–244.
31. Ramírez, E.; José, H.; Oria, E. Division and new multiplication between vectors. *arXiv* **2023**, arXiv:2301.12078. [CrossRef]
32. Li, Z.; Su, H.; Zhou, S.; Hu, Q. Double-threshold CFAR detector in presence of subspace interference for MIMO radar. *IET Signal Process.* **2019**, *14*, 72–80. [CrossRef]
33. Subramanyan, N.; Kalpathi, R.; Vengadarajan, A. Robust variability index CFAR for non-homogeneous background. *IET Radar. Sonar Navig.* **2019**, *13*, 1775–1786. [CrossRef]